Guidance and Control Design for the Ascent phase of the Hopper RLV

Andrés Marcos[*] and Luis F. Peñín.[†]
Deimos Space S.L., Madrid, 28760, Spain

Josef Sommer[‡], Wolfgang Belau[§]
Astrium Space Transportation, Bremen, 28199, Germany

Eric Bornschlegl[**]
ESA ESTEC, Noordwijk, 2200, The Netherlands

In this article the design of a guidance and control system for the automated ascent of the Hopper reusable launch vehicle is presented. The considered ascent starts at the pull-up maneuver performed immediately after horizontal take off and ends near main-engine-cut-off. The guidance (trajectory control) law is based on the coupled inversion of flight-path-to-angle-of-attack and heading-to-bank-angle dynamics. The control (attitude) law uses also nonlinear dynamic inversion to obtain the required aerodynamic surfaces and engine gimbal deflections for robust tracking of the attitude angles from the guidance law. The used NDI attitude law is inherited from a previous design for the Hopper re-entry phase (with only minor modifications apart from the inclusion of thrust vector control) showcasing the reusability of NDI designs for quite different types of configurations. The resulting design has been validated using a Monte Carlo campaign with realistic aerodynamic mismatch, corrupted measurements, parametric uncertainty and high fidelity atmospheric and 6DoF vehicle dynamics models.

Nomenclature

α	=	Angle of attack,
β	=	Angle of sideslip
χ	=	Heading angle
δ	=	Latitude
$\delta y/z_{-eng}$	=	Engine gimbal deflections for pitch (δy_{eng}) and yaw (δz_{eng})
$\delta_\bullet$	=	Aerodynamic surface deflections, • = ERO/ELO (elevon right/left outboard), ERI/ELI (inboard), RUD (rudder), SB (speedbrake) and FLAP
γ	=	Flight path angle
σ	=	Bank angle
Ω_E	=	Earth's angular velocity
$a^B_{X/Y/Z}$	=	Body-axes x/y/z accelerations
g	=	Earth's gravity
m	=	Spacecraft mass
M	=	Mach number
$M_\bullet$	=	Moment (in the direction / component indicated by •, e.g. $M_{Xeng\text{-}1}$ is the x-axis moment for engine number 1)
R	=	Distance between Earth's center and the spacecraft's center of gravity
$Tn_{1/2/3}$	=	Thrust for engines 1/2/3
$s_\bullet$,$c_\bullet$	=	Sine and cosine of angle indicated by •

[*] Senior Control Engineer, Deimos Space S.L. Email: andres.marcos@deimos-space.com
[†] Project manager and section head, Deimos Space S.L., and AIAA Senior Member.
[‡] Project Manager, EADS-Astrium Space Transportation.
[§] Senior Engineer, EADS-Astrium Space Transportation.
[**] Technical Officer, ESA ESTEC.

Introduction

IN this article the design of a nonlinear dynamic inversion (NDI) guidance and control (G&C) system for the ascent phase of the Hopper Reusable Launch vehicle (RLV) is described. The ascent phase considered starts at the pull-up maneuver performed immediately after horizontal take off and ends close to main-engine-cut-off (MECO). The design is part of the European Space Agency (ESA) "Health Management Systems for Reusable Launch Vehicles" project lead by EADS-Astrium (Germany) with the objective of assessing, developing and testing HMS and fault detection and isolation (FDI) algorithms for all the RLV main (G&C, engines and structural) components. Deimos Space tasks in the HMS project are the development of the consortium's closed-loop assessment environment (conformed principally by a functional engineering simulator, FES, and the G&C designs) and also of developing the G&C FDI algorithms [8].

The selection of NDI [3, 6, 7, 13, 15] as the design technique behind the re-entry / ascent G&C components was motivated by the need to provide a common G&C architecture for both phases and also to provide some natural closed-loop fault tolerant control (FTC) properties. The first need arises from programmatic time and cost issues, while the second is the result of a desire to have wide fault coverage: from incipient faults (not detectable with very robust/FTC G&C designs [9]) to hard/strong faults (which, without a G&C providing some closed-loop FTC properties, result in almost immediately closed-loop instability impeding FDI assessment and verification).

In [10] the re-entry control design for the HMS project is presented, it uses a mixed wind-body formulation for the atmospheric re-entry vehicle but no outer-loop guidance (i.e. trajectory control) yielding acceptable results albeit with some robustness issues (i.e. dispersion on guidance flight-path / heading angles tracking with a few unstable cases –arising from body accelerations undamped divergence). The re-entry attitude control design in [10] forms the basis of the ascent G&C architecture presented in this article.

The proposed ascent G&C architecture developed is characterized by:

1) An NDI-based guidance law using flight path γ_{ref} and heading χ_{ref} reference angles to calculate control reference angles: angle of attack α_{calc}, sideslip β_{calc} and bank angle σ_{calc};
2) An NDI-based attitude control loop consisting of fast (inner) and slow (outer) loops that use the previous calculated control reference angles to estimate desired ideal moments;
3) A moment allocation scheme that distributes the estimated desired moments to the dynamic inversion schemes of the aerodynamic surface and thrust vector control (TVC).
4) An aerodynamic moment dynamic inversion component that obtains the desired aerodynamic control surface deflections based on the allocated aerodynamic moments;
5) A thrust vector control (TVC) that calculates pitch and yaw gimbal deflections for each of the three Hopper engines using the allocated moment and the available thrusts per engine.

The resulting ascent NDI G&C (plus TVC) design is validated using the developed high-fidelity closed-loop Hopper FES in a Monte Carlo campaign (with varying parametric and aerodynamic coefficients uncertainties). The results indicate that the G&C design successfully achieves the desired design objectives and improves the robustness of the closed-loop (in comparison with the re-entry control design, which lacked the guidance component).

Reference scenario: Ascent phase of the Hopper RLV

The selected reference vehicle and scenario is that of the Hopper, an evolution from the FESTIP study further elaborated in the scope of the ASTRA program [14]. The Hopper mission is to execute sub-orbital point -to-point flights for delivery of orbital payloads. The mission sequence is: to accelerate the payload to prescribed sub-orbital staging conditions, ejection of the cargo, drift to ~150 km altitude, automated atmospheric re-entry and glide to the selected landing site (some 4500 km downrange depending on mission inclination). The duration of a Hopper flight is less than half an hour from horizontal take-off until the vehicle arrives over the downrange landing site.

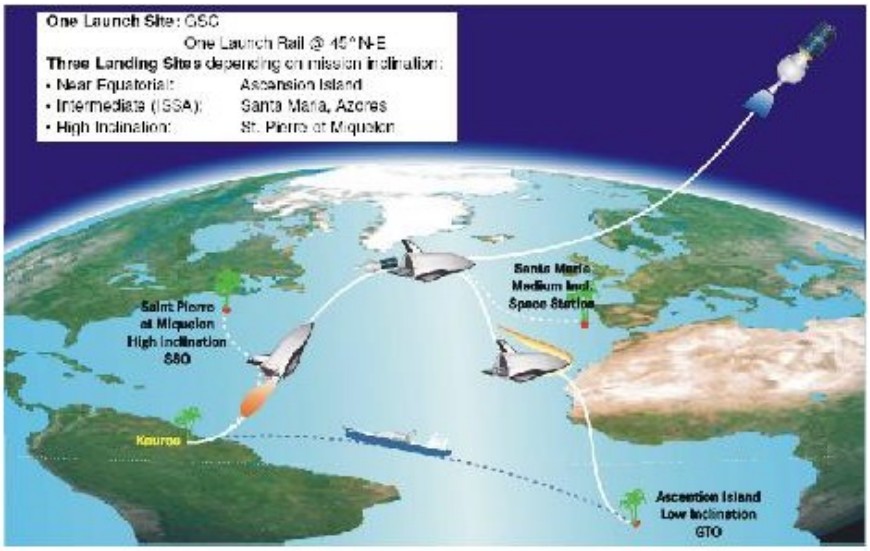

Figure 1 EADS-ST Hopper mission profile

The phase of interest for the HMS ascent G&C design starts from the moment the Hopper has initiated the pull-up manoeuvre after the horizontal sled-driven take off and ends at around 85 Km of altitude and Mach 16 (just prior to MECO). Figure 2 shows the main rotational and aerodynamic profiles for the reference ascent trajectory.

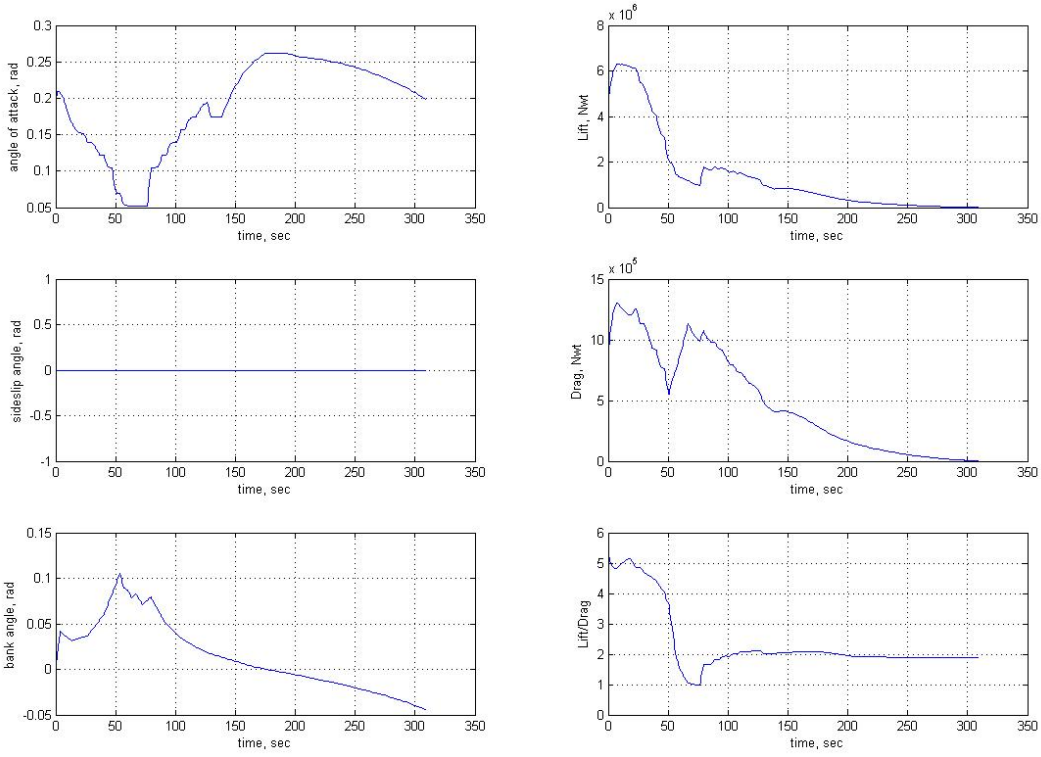

Figure 2 Ascent reference trajectory – rotational and aerodynamics parameters

The G&C design objectives consist in robust and accurate tracking of the reference guidance (γ_{ref}, χ_{ref}) and calculated aerodynamic (α_{calc}, β_{calc}, σ_{calc}) angles, reduced control activity and stability throughout the flight despite the presence of parametric uncertainty, sensor noise and aerodynamic mismatch. Table 1 summarizes the main design objectives (MRP stands for mean-reference-point):

Table 1 Ascent design objectives

γ, χ, α, β, σ Tracking error	Less than +/- 2 degrees
Angle of attack	Magnitude limited to 18deg < α < 38deg for M > 10 and perturbations eliminated in <10 seconds
Bank rate & acceleration	Bank rate shall be higher than 15deg/s and acceleration higher than 5 deg/s/s
Control effectors	Reduced control actuation activity
Robustness	Shall be robust to: ▪ Sensor noise ▪ Aerodynamic mismatch (see percentage profiles in Figure 3) ▪ Parametric uncertainty Mass 5%; Ixx, Iyy, Izz 5%; x, z-MRP 0.5%; y-MRP 0.1%

The main challenges for the Hopper ascent G&C design are the result of the large dynamical changes (e.g. from Mach 0 to 16), the large mass variation occurring from the engine fuel consumption (a change from 491,288 kg down to 90,000 kg) and the mass variation effect on the moment of inertia and center-of-gravity. In addition to the mass variation and dynamic changes, system uncertainty from parametric and aerodynamic mismatch is also considered. The uncertainty is modeled using a multiplicative formulation [1] that allows defining the uncertainty in terms of percentage variations with respect to nominal values.

The parametric uncertainty arises due to imperfect knowledge of the actual mass, moments of inertia and MRP coordinates (equivalent to center-of-gravity coordinates uncertainty). The aerodynamic mismatch is introduced to recreate the uncertainty that exists in the calculation of aerodynamic databases, which are intrinsically very difficult to identify, and to avoid perfect cancellation of the dynamics (due to the inversion effect of the NDI controllers). Typically, constant percentage changes are applied to the aerodynamic coefficients and/or stability derivatives but sometimes, and more accurately, Mach or altitude based percentage profiles can be used as well as more physical functional constraints between them, e.g. Lift-to-Drag-ratio uncertainty to correct those for the Lift and Drag. **Figure 4** shows the aerodynamic coefficients' uncertainty profiles used to perturb the Hopper aerodynamic database (note the inclusion of L/D uncertainty for the aforementioned reason). These profiles scale the aerodynamic coefficients during the subsequent assessment campaign –it is highlighted that the profiles change with Mach so that for a specific Monte-Carlo case the aerodynamic uncertainty is dynamically changed as the simulation progresses.

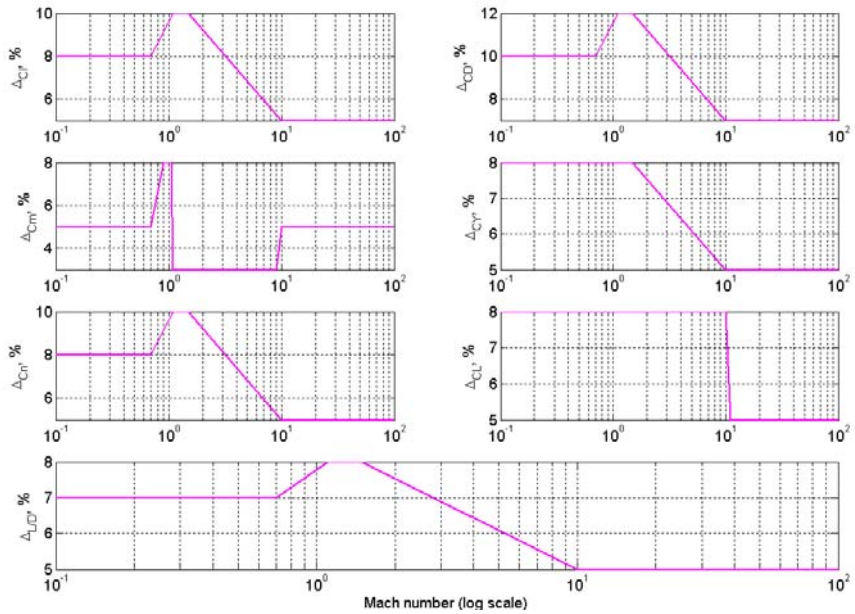

Figure 3 Aerodynamic coefficients percentage uncertainty profiles.

An additional challenge (especially in comparison to that for the unpowered re-entry) arises from the engine thrust output and gimballing, which requires the design of a thrust vector control unit within the attitude control component of the ascent G&C. The Hopper RLV has three Snecma Vulcain main engines that can be gimbaled independently (i.e. each with its own actuator system) in pitch and yaw directions, see **Figure 4**:

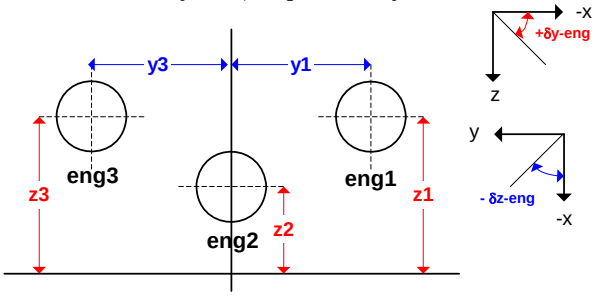

Figure 4 Hopper engines position (from rear view) and deflection angle sign convention.

For each engine, the actual engine forces are calculated based on the provided thrust *Tn* and the corresponding engine gimbal deflections. In body frame, the engine forces are expressed as in Eq. 1 (to calculate the total body-axes forces, the engine forces are transformed to wind-axes prior to being added to the aerodynamic forces):

$$F_{eng} = \begin{bmatrix} F_{Xeng} \\ F_{Yeng} \\ F_{Zeng} \end{bmatrix} = \begin{bmatrix} Tn\cos\delta y_{eng}\ \cos\delta z_{eng} \\ Tn\cos\delta y_{eng}\ \sin\delta z_{eng} \\ -Tn\sin\delta y_{eng} \end{bmatrix} \qquad \textbf{Eq. 1}$$

The engine moments are calculated using the body-axes engine forces and the moment-arm given by the distance measured from the engine nozzle reference point to the center of gravity, i.e. $r=r_{nozzle}-r_{cg}=[x_{eng}\ \ y_{eng}\ \ z_{eng}]$:

$$M_{eng} = \begin{bmatrix} y_{eng}\cdot F_{Zeng} - z_{eng}\cdot F_{Yeng} \\ z_{eng}\cdot F_{Xeng} - x_{eng}\cdot F_{Zeng} \\ x_{eng}\cdot F_{Yeng} - y_{eng}\cdot F_{Xeng} \end{bmatrix} = \begin{bmatrix} 0 & -z_{eng} & y_{eng} \\ z_{eng} & 0 & -x_{eng} \\ -y_{eng} & x_{eng} & 0 \end{bmatrix} \begin{bmatrix} F_{Xeng} \\ F_{Yeng} \\ F_{Zeng} \end{bmatrix} \qquad \textbf{Eq. 2}$$

It is noted that the matrix in the right-most term of Eq. 2 has no inverse (an important consideration if NDI techniques are directly used for thrust vector control).

Ascent NDI control law design

This section presents the attitude control law design including the thrust vector control component, which is represented by the highlighted box in Figure 5, the general Hopper ascent G&C architecture.

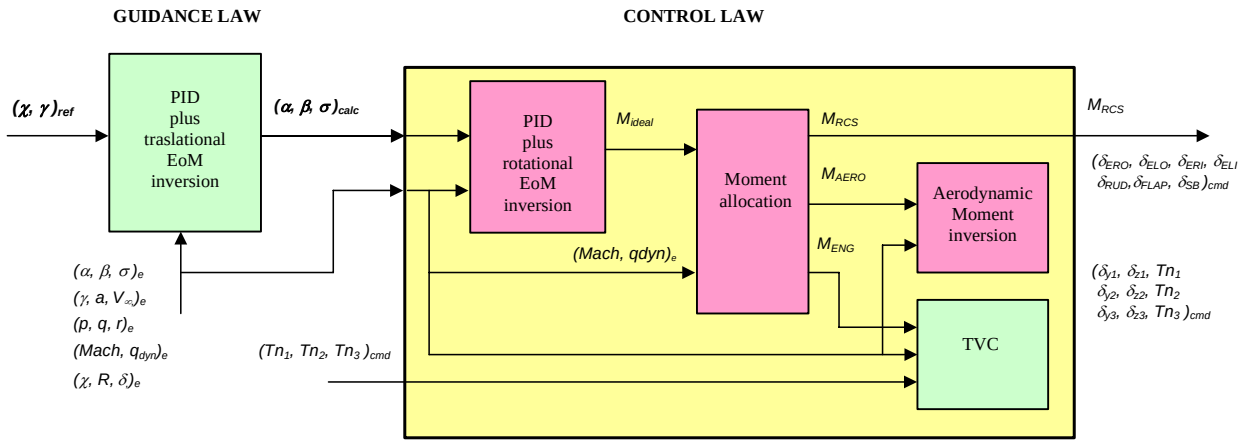

Figure 5 Ascent NDI G&C architecture.

From Figure 5 it is seen that the control law block is composed of four major components: a *PID-plus-Rotational-EoM-Inversion* component that estimates desired (ideal) moments based on the calculated aerodynamic angles from the guidance law; a *Moment-Allocation* block in charge of distributing these estimated ideal moments to the appropriate effectors (aerodynamic surfaces, thrust vector control system and reaction control system –although for the latter direct feed through is assumed with only magnitude and rate saturation limiters); an *Aerodynamic-Moment-Inversion* component that transforms the aerodynamic ideal moments into commanded aerodynamic control surface deflections; and the *TVC* component, which uses the allocated engine ideal moments (and available engine thrusts) to calculate the required engine gimbals' deflections per engine. Each of these four elements is described next:

A. PID-plus-Rotational-EoM-Inversion component

This block provides the ideal moments required to fulfill the control performance and stability objectives. It uses a four-step approach implementing an outer (slow) attitude control-loop, that transforms the calculated aerodynamic angles into desired rotational-rates derivatives, and an inner (fast) attitude control-loop that uses these desired derivatives to obtain desired moments. Each of these two loops contain a set of PID gains that establish the natural frequency and damping for each of the channels (the term PID is used for generality purposes since some of the final sets only consider proportional gains). The PID gain sets are scheduled on Mach and dynamic pressure reflecting the varying dynamics of the Hopper vehicle and mission.

This component is taken, without modification or gain re-tuning, from the Hopper re-entry control design, see [10] for further details.

B. Moment-Allocation component

This component distributes the ideal moments obtained in the previous PID-based block to the aerodynamic, RCS or TVC effector inversion schemes. It also commands the switching among the previous PID-gain sets.

Five allocation phases are defined, the first two based on Mach number and the last three phases on dynamic pressure thresholds. These allocation phases are not optimally defined to satisfy effector activity minimization or fault tolerance objectives, rather they simply distribute the total moments using constant or smooth scaling functions based on the two scheduling variables (Mach and dynamic pressures).

C. Aerodynamic-Moment-Inversion component

This is the most well-known and standard component in NDI approaches. Its purpose is to transform the ideal aerodynamic moments M_{AERO} assigned in the previous component into control aerodynamic surface deflections.

The aerodynamic inversion scheme for the ascent G&C is also taken from the re-entry controller design [10]. The only difference with respect to the re-entry block is that during the ascent phase the rate and magnitude limits of the aerodynamic effectors are modified based on Mach and dynamic pressure. This modification enforces more restrictive aerodynamic actuator limits to avoid saturation or large deflections at high speeds or during specially challenging parts of the ascent trajectory.

This component consists of three sub-blocks: one for estimation of the aerodynamic coefficients and two for inversion (one for the so-called FLIGHT control effectors and the other for those referred to as TRIM). The latter set of effectors is typically used to achieve aerodynamic trim (i.e. zero out moments) and is composed of flap (δ_{FLPA}), rudder (δ_{RUD}) and inboard elevons (δ_{ERI} and δ_{ELI}) –with the FLIGHT effectors being composed of the remaining surfaces (outboard) and a subset of those for TRIM.

D. Thrust-Vector–Control component

This component represents a major innovative component of the Hopper vehicle for G&C development. The redundancy offered by the three engines provides a certain level of fault tolerance to engine faults but also to aerodynamic actuator faults (by providing an additional moment effector capability).

The TVC pertains only the calculation of the engine gimbal deflections required to achieve the desired allocated engine moments (that is, it does not provide thrust modulation control). The approach and implementation used is developed with the goal to simplify the design of the TVC system but also looking for means to naturally provide some inherent fault accommodation capabilities (taking advantage of the offered engine redundancy).

The first step is to combine the equations for the body-axes engine forces from Eq. 1 and that for the moments Eq. 2 to yield the engine moments for a specific engine in terms of its thrust and gimbal deflections Eq. 3. Assume, based on the maximum gimbals deflection of ±14 degrees, that the trigonometric expressions can be approximated using small angle assumptions to finally yield:

$$\begin{bmatrix} M_{Xeng} \\ M_{Yeng} \\ M_{Zeng} \end{bmatrix}_{eng-i} = \begin{bmatrix} -Tn(y_{eng}\sin\delta y_{eng} + z_{eng}\cos\delta y_{eng}\sin\delta z_{eng}) \\ Tn(z_{eng}\cos\delta y_{eng}\cos\delta z_{eng} + x_{eng}\sin\delta y_{eng}) \\ Tn(x_{eng}\cos\delta y_{eng}\sin\delta z_{eng} - y_{eng}\cos\delta y_{eng}\cos\delta z_{eng}) \end{bmatrix}_{eng-i}$$
$$\approx \begin{bmatrix} -Tn(y_{eng}\delta y_{eng} + z_{eng}\delta z_{eng}) \\ Tn(z_{eng} + x_{eng}\delta y_{eng}) \\ Tn(x_{eng}\delta z_{eng} - y_{eng}) \end{bmatrix}_{eng-i} \qquad \textbf{Eq. 3}$$

Next, summing the contribution from each engine and re-arranging in the unknown gimbal deflections, the total engine moments are obtained:

$$\begin{bmatrix} M_{Xeng} \\ M_{Yeng} \\ M_{Zeng} \end{bmatrix} = \sum_{i=1}^{3} \begin{bmatrix} -Tn\cdot y_{eng} & -Tn\cdot z_{eng} \\ Tn\cdot x_{eng} & 0 \\ 0 & Tn\cdot x_{eng} \end{bmatrix}_i \begin{bmatrix} \delta y_{eng} \\ \delta z_{eng} \end{bmatrix}_i + \begin{bmatrix} 0 \\ \sum_{i=1}^{3} Tn_i \cdot z_{eng-i} \\ -\sum_{i=1}^{3} Tn_i \cdot y_{eng-i} \end{bmatrix} \qquad \textbf{Eq. 4}$$

Eq. 4 can be simplified using the engines position symmetry, see **Figure 4**: $x_{eng1} = x_{eng2} = x_{eng3}$, $y_{eng1} = -y_{eng3}$, $z_{eng1} = z_{eng3}$ and $y_{eng2} = 0$.

$$\begin{bmatrix} M_{Xeng} \\ M_{Yeng} \\ M_{Zeng} \end{bmatrix} = \begin{bmatrix} -Tn_1 y_{eng1} & -Tn_1 z_{eng1} & 0 & -Tn_2 z_{eng1} & -Tn_3 y_{eng1} & -Tn_3 z_{eng1} \\ Tn_1 x_{eng1} & 0 & Tn_2 x_{eng1} & 0 & Tn_3 x_{eng1} & 0 \\ 0 & Tn_1 x_{eng1} & 0 & Tn_2 x_{eng1} & 0 & Tn_3 x_{eng1} \end{bmatrix} \begin{bmatrix} \delta y_{eng1} \\ \delta z_{eng1} \\ \delta y_{eng2} \\ \delta z_{eng2} \\ \delta y_{eng3} \\ \delta z_{eng3} \end{bmatrix} \qquad \textbf{Eq. 5}$$
$$- \begin{bmatrix} 0 \\ z_{eng1}(Tn_1 + Tn_3) + z_{eng2} Tn_2 \\ y_{eng1}(Tn_3 - Tn_1) \end{bmatrix} = A\Gamma - B$$

The standard NDI approach proceeds by calculating matrices A and B in Eq. 5 using the measured thrusts, subtracting the obtained B from the total allocated engine moments M_{eng} and left-multiplying the result by the inverse of A as shown in Eq. 6:

$$\Gamma = \boldsymbol{W} \cdot \left[\boldsymbol{AW}\right]^{+} (\boldsymbol{M} + \boldsymbol{B}) \qquad \textbf{Eq. 6}$$

Where $[\bullet]^{+}$ indicates Moore-Penrose pseudo inverse and W is a regularization matrix used to avoid ill conditioning (but that can be used as well as a tuning parameter to adequately weight the problem or for allocation issues [6, 5]).

This standard approach was used first and good results were obtained for the initial phase of the ascent but with incremental tuning difficulty when PID-gains / moment allocation switching phases were considered. Furthermore, although the nature of the NDI approach provides some level of fault accommodation it is not straightforward to include some reconfiguration-tuning provision. Additionally and more importantly, it was noted before that the matrix in Eq. 5 has no inverse and thus numerical issues regarding regularization (i.e. use of appropriate W) must be carefully considered to avoid singularities, thus resulting in a more complex design and validation process.

Based on the above remarks, a different NDI-TVC approach is used that facilitates comprehension and design of the resulting TVC system (especially for fault purposes). The approach is based on performing an additional TVC-internal allocation phase of the desired engine moments (obtained from the Moment-Allocation block) and subsequently following a sequential inversion scheme to calculate the engine gimbal deflections. The latter sequential inversion scheme performs first the individual dynamic inversion for each of the two portside (i.e. symmetric) engines and subsequently that for the central engine –using for the latter engine, desired moments calculated based on the difference between the ideal total allocated engine moments and the achievable portside

engine moments. Note that the achievable portside moments calculation is affected by the gimbal actuators health information from the HMS/FDI system. The following steps summarize the (fault tolerant) NDI TVC approach:

- **Step 1**: Distribute the allocated engine moments between the portside engines (engine 1 and 3 in **Figure 4**).
- **Step 2**: Use dynamic inversion to calculate (independently) the portside engines gimbal deflections. It is noted that the inversion is very straightforward due to the symmetry and specific engine positions.
- **Step 3**: Estimate the actual achievable portside engine moments and use these estimates together the total engine allocated moment to calculate the required moment for engine 2.
- **Step 4**: Calculate engine 2 gimbal deflections using the allocated moment from the previous step in a similar manner to Step 2.

Note, that in the above TVC NDI design process, information from the HMS/FDI system regarding the health status of the gimbal actuators can be used in steps 1,2 and 4 (the availability of this information is indeed the basis of the TVC approach which relies in the interpretation of NDI as an achievable dynamic estimation process [12]).

Ascent guidance law

Guidance laws are primarily concerned with the definition of optimal trajectories that fulfill fuel-minimization, heat/gravity/path objectives and arrive at desired exit conditions (in the case of ascent vehicles). Secondarily, the guidance should be designed to 'help' the attitude control system to achieve robust performance objectives. Indeed, it can be argued that in general, a control system tries to make the closed-loop behave as a linear system and the guidance tries to adapt the trajectory to behave as a trim-corrected input thus helping the control to keep the system in a linear regime. Any guidance system is typically decomposed into two components: one generating the optimal trajectory and the other calculating the desired control references from this optimal trajectory.

In this section, the focus is on the second component: developing a longitudinal and lateral/directional guidance law to calculate the control references (angle of attack α_{calc}, bank angle σ_{calc} and sideslip angle β_{calc}) based on an optimal trajectory composed of flight path γ_{ref} and heading χ_{ref} angles. For longitudinal trajectory control, also referred to as vertical guidance, a *γ-steering-with-α-control* guidance is used while for lateral/directional trajectory control an approach based on *χ-steering-with-σ-control* is proposed. Both guidance systems rely on the use of dynamic inversion and assume sideslip angle is ideally zero (a standard desired design objective for high-speed vehicles such as RLVs).

The translational dynamic equations of motion for an RLV can be given in detail using spherical position and velocity coordinates, but for convenience only those for the heading and flight-path angle are given here (dropping negligible terms containing $R\Omega_E^2$):

$$\dot{\chi} = \frac{F_\chi}{Vm\cos\gamma} + 2\,\Omega_E\left(\sin\delta - \cos\delta\tan\gamma\cos\chi\right) + \frac{V}{R}\tan\delta\cos\gamma\sin\chi = \frac{F_\chi}{Vm\cos\gamma} + \mathrm{B}_\chi \qquad \textbf{Eq. 7}$$

$$\dot{\gamma} = \frac{F_\gamma}{Vm} + 2\,\Omega_E\,\sin\chi\cos\delta + \frac{V}{R}\cos\gamma = \frac{F_\gamma}{Vm} + \mathrm{B}_\gamma \qquad \textbf{Eq. 8}$$

The external forces F_γ and F_χ can be expressed in terms of the wind forces F_{wx}, F_{wy} and F_{wz} and the gravitational force F_g to yield:

$$F_\gamma = F_{wy}\sin\sigma - F_{wz}\cos\sigma - F_g\cos\gamma \qquad \textbf{Eq. 9}$$

$$F_\chi = F_{wy}\cos\sigma + F_{wz}\sin\sigma \qquad \textbf{Eq. 10}$$

One singularity arises in the above equations, when the flight-path-angle γ becomes equal to ±90º. In the considered ascent scenario this condition will not occur since for the used nominal trajectory the maximum flight path angle is around 47 degrees. Also, note that the heading and flight-path angle rates are coupled through the wind-axes forces and the bank angle σ.

Most vertical guidance algorithms assume that the bank angle is zero and then derive the desired reference angle of attack based on a γ-rate desired value –generated using the error from the given and measured γ. Alternatively, they simplify the above equations quite strongly and use two-point boundary optimization to obtain the reference angles of attack and bank. Furthermore, they typically express the external forces in terms of Drag and Lift forces and approximate these in terms of drag polar look-up tables and angle of attack –which requires quite accurate knowledge on the drag and lift characteristics (not usually the case except after long and expensive wind-tunnel,

CFD and flight testings). The approach used differentiates itself in that it relies in more easily accessible (i.e. measurable) signals, keeps the coupling from the equations of motion and calculates the optimal reference control angles without requiring an optimization algorithm (but relying in an optimally generated trajectory, which is always the case in most of the other algorithms). Additionally, it has a strong classical and flight mechanic/control interpretation [11] that helps understand which terms to simplify and how to tune the resulting gains.

First, note that dividing the wind forces by mass and using the transformation matrix from body to wind axes it is straightforward to express the external forces in terms of body-axis accelerations (which are easily measurable signals by means of accelerometers placed at the center of gravity):

$$\begin{bmatrix} \frac{F_\gamma}{m} \\ \frac{F_\chi}{m} \end{bmatrix} = \begin{bmatrix} -s_\sigma & -c_\sigma \\ c_\sigma & -s_\sigma \end{bmatrix} \begin{bmatrix} -c_\alpha s_\beta & c_\beta & -s_\alpha s_\beta \\ -s_\alpha & 0 & c_\alpha \end{bmatrix} \begin{bmatrix} a_X^B \\ a_Y^B \\ a_Z^B \end{bmatrix} - \begin{bmatrix} gc_\gamma \\ 0 \end{bmatrix} \qquad \textbf{Eq. 11}$$

In the above expression, shorthand is used for the trigonometric functions to alleviate notation. Assuming small angles (acceptable looking at the reference trajectory in Figure 2) and substituting the resulting external forces in the heading and flight-path angle rate equations from Eq. 7and Eq. 8 yields:

$$V\dot{\gamma} = \alpha\, a_X^B - \sigma\, a_Y^B - a_Z^B - gc_\gamma + V\mathrm{B}_\gamma \qquad \textbf{Eq. 12}$$

$$Vc_\gamma \dot{\chi} = \alpha\sigma\, a_X^B + a_Y^B - \sigma\, a_Z^B + Vc_\gamma \mathrm{B}_\chi \qquad \textbf{Eq. 13}$$

Now, inverting the γ-rate equation and grouping terms the calculated angle of attack α_{calc} is obtained:

$$\alpha_{cal} = \frac{V}{a_X^B}\dot{\gamma}_{des} + \frac{a_Z^B + gc_\gamma}{a_X^B} - \frac{V\mathrm{B}_\gamma}{a_X^B} + \frac{\sigma\, a_Y^B}{a_X^B} = K_1^\gamma \dot{\gamma}_{des} + K_2^\gamma - K_3^\gamma + K_4^\gamma \qquad \textbf{Eq. 14}$$

Note that the gain K^γ_1 is the actual γ-rate-to-α, K^γ_2 represents the trim value of α at which the γ-rate is zero (i.e. when aerodynamic, thrust and gravity effects in the longitudinal plane are balanced), K^γ_3 represents the influence of Coriolis and centrifugal accelerations and K^γ_4 is the coupling effect with the lateral/directional component. The desired γ-rate is obtained, in general form, using a proportional-derivative-integrating (PID) controller of the error between the reference γ_{ref} and the measured γ_{meas} signals.

$$\dot{\gamma}_{des} = K_P^\gamma(\gamma_{des} - \gamma_{meas}) + K_D^\gamma(\gamma_{des} - \gamma_{meas}) + K_I^\gamma(\gamma_{des} - \gamma_{meas}) \qquad \textbf{Eq. 15}$$

In the guidance implementation, the gain K^γ_4 is dropped since its contribution is negligible compared to the other longitudinal components (expected since any RLV control system should minimize lateral acceleration and moreover, since bank angle is relatively small $|\sigma| \leq 6$ degrees for the ascent trajectory). Also, the measured γ-rate is used in feed forward to improve the system response (especially necessary since only proportional and derivative gains are used in Eq. 15).

From the above remarks, it is seen that the longitudinal guidance law is independent of the bank angle due to the small contribution of this angle when multiplied by the lateral acceleration. Nevertheless, this term could be used to improve system response when unexpected sideslip deviations occur. On the other hand, the bank guidance law should be derived to depend on the longitudinal angle of attack since it highly depends on longitudinal accelerations, from Eq. 13 the following calculated bank angle formula is similarly obtained:

$$\sigma_{calc} = \frac{Vc_\gamma}{\alpha\, a_X^B - a_Z^B}\dot{\chi}_{des} - \frac{a_Y^B}{\alpha\, a_X^B - a_Z^B} - \frac{Vc_\gamma \mathrm{B}_\chi}{\alpha\, a_X^B - a_Z^B} = K_1^\chi \dot{\chi}_{des} - K_2^\chi - K_3^\chi \qquad \textbf{Eq. 16}$$

Similar to the γ-steering-with-α-control, the gain K^χ_1 gives the actual χ-rate-to-σ while the other two gains represent the lateral/directional acceleration and the Coriolis/centrifugal acceleration terms respectively. In this case, the gain K^χ_2 is extremely important since the calculated bank angle should include the sideslip coupling, which is critical for control despite sideslip being considered ideally zero (in other words, since sideslip control is open-loop guided the calculated bank angle must absorb the deviations and transients arising from any sideslip error).

The direct implementation of the heading-steering law from Eq. 16 is problematic due to the use of longitudinal accelerations. It results in too much oscillatory behaviour that would require for practical usage smoothing all the accelerations (only the lateral acceleration a^B_Y was finally required, and smoothed using a 1st order low-pass filter with time constant of 10 seconds –equivalent to using a least squares smoothing filter of the acceleration signal with a 10 second window). To avoid using all the accelerations, with the associated loss in precision from the smoothing

filters, and at the same time improving the coupling between the calculated bank angle and the longitudinal guidance law, the following substitution is used arising from manipulation of the γ-rate of Eq. 12:

$$\alpha\, a_X^B - \sigma\, a_Y^B - a_Z^B = V\dot{\gamma}_{des} + gc_\gamma - \sigma\, a_Y^B - VB_\gamma \qquad \textbf{Eq. 17}$$

In the final implementation, see Figure 6, the term VB_γ is dropped (although it can be used to improve the response) and the term $\sigma\, a^B{}_Y$ is transformed into $\sigma^2\, a^B{}_Y$ when substituted into Eq. 14 and thus considered also negligible due to the $|\sigma| \le 6$ degrees magnitude. Thus, the final lateral/directional guidance law is given by:

$$\sigma_{calc} = \frac{Vc_\gamma}{V\dot{\gamma}_{des} + gc_\gamma}\dot{\chi}_{des} - \frac{a_Y^B}{V\dot{\gamma}_{des} + gc_\gamma} - \frac{Vc_\gamma B_\chi}{V\dot{\gamma}_{des} + gc_\gamma} = K_1^\chi \dot{\chi}_{des} - K_2^\chi - K_3^\chi \qquad \textbf{Eq. 18}$$

As above, the desired χ-rate is obtained using a PID system on the error between the reference χ_{ref} and measured heading angles χ_{meas}. Figure 6 shows the ascent guidance law architecture (the heading hat-gains indicate that only their numerators are used, i.e. they are constants –with the denominator being included afterwards as shown).

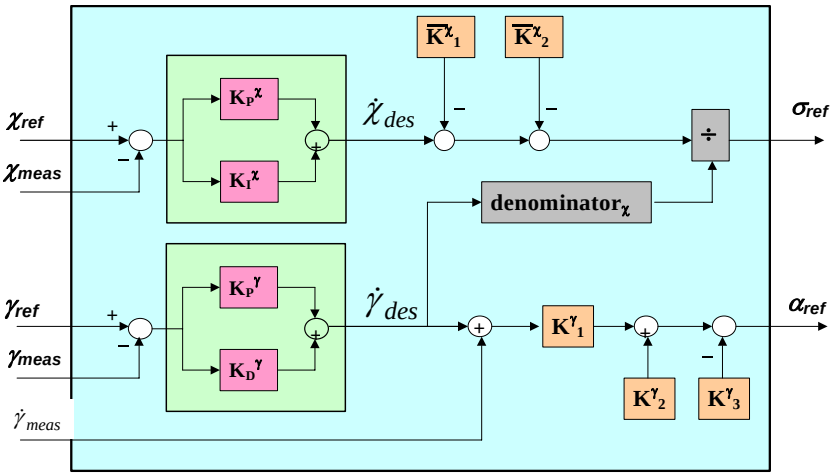

Figure 6 Ascent NDI guidance law implementation

Closed-loop Time Responses Evaluation

In this section the performance and robustness of the NDI G&C design in tracking the reference ascent nominal trajectory is evaluated. A Monte-Carlo (MC) analysis using random perturbation of the uncertainty set (formed by the parametric and aerodynamic database uncertainty given before) is performed for 1500 runs. The simulation environment used (i.e. the closed-loop assessment FES) has the following features:

- Full 6 DoF nonlinear RLV dynamics and high-fidelity EADS-Astrium Hopper aerodynamic database.
- 1962 USA atmospheric and ellipsoid planet shape models.
- The actuators are always magnitude and rate limited. The aerodynamic and engine gimbal actuators include also 2nd order actuator dynamics (the RCS is assumed to be direct feed through).
- Each simulation run is completely automated (i.e. no phase patching is performed for the entire ascent trajectory considered). This is an important consideration that showcases the effectiveness of the controller for complete automated control of the ascent trajectory.
- Sensor measurements are colored noise corrupted (except for the accelerometers, which use white noise corruption), following the models given in [10].
- A reference total thrust profile is used, equally split for each of the three Hopper engines. Test with the high-fidelity Snecma engine models were also performed for a selected set of uncertainty scenarios and yielded satisfactory results (the engine model time constant does not allow for intensive MC campaign.)
- For each MC run, a random variable (all uniformly distributed between ±1 and using different seeds) is obtained for each aerodynamic coefficient and is used to scale the profiles shown in **Figure 3**. Furthermore, in order to physically motivate the uncertainty, the lift and drag uncertainties thus obtained are compared, and re-calculated if needed, to the Lift-to-Drag ratio uncertainty obtained from randomly scaling the profile

at the bottom of **Figure 3**. This will ensure that no unrealistic Lift and Drag coefficient uncertainty is obtained (see [2] for more details).

- In all the simulation results presented, the first two seconds are removed to discard simulation initialization transients (this is without consequences in the analysis).

Figure 7 presents the time responses of the measured guidance angles (χ, γ), aerodynamic angles (α, β, σ) and their errors with respect to the corresponding reference signals (γ_{ref}, χ_{ref}, α_{calc}, β_{calc} and σ_{calc}) for 300 of the 1500 MC runs performed (only 300 due to the high figure Bit-size obtained otherwise). Note, that the guidance reference angles are those from the optimized ascent trajectory while the aerodynamic angles are obtained from the guidance law (and thus are not fixed profiles as χ_{ref} and γ_{ref}). This implies that the plots in the left of Figure 7 corresponding to the aerodynamic angles time responses show a larger spread than those for the guidance (although the error plots in the right indicate that the NDI G&C performs very well for all). The performance objectives are given by dotted lines in the error plots (i.e., the responses in the right-plots should not be greater than 2 degrees as stipulated in Table 1). Note that all error responses show quite good satisfaction of the tracking tasks (it is highlighted that this stems also from the inclusion of the G in the G&C design since for the re-entry control design –which lacked a guidance law—the results showed large guidance error responses [10])

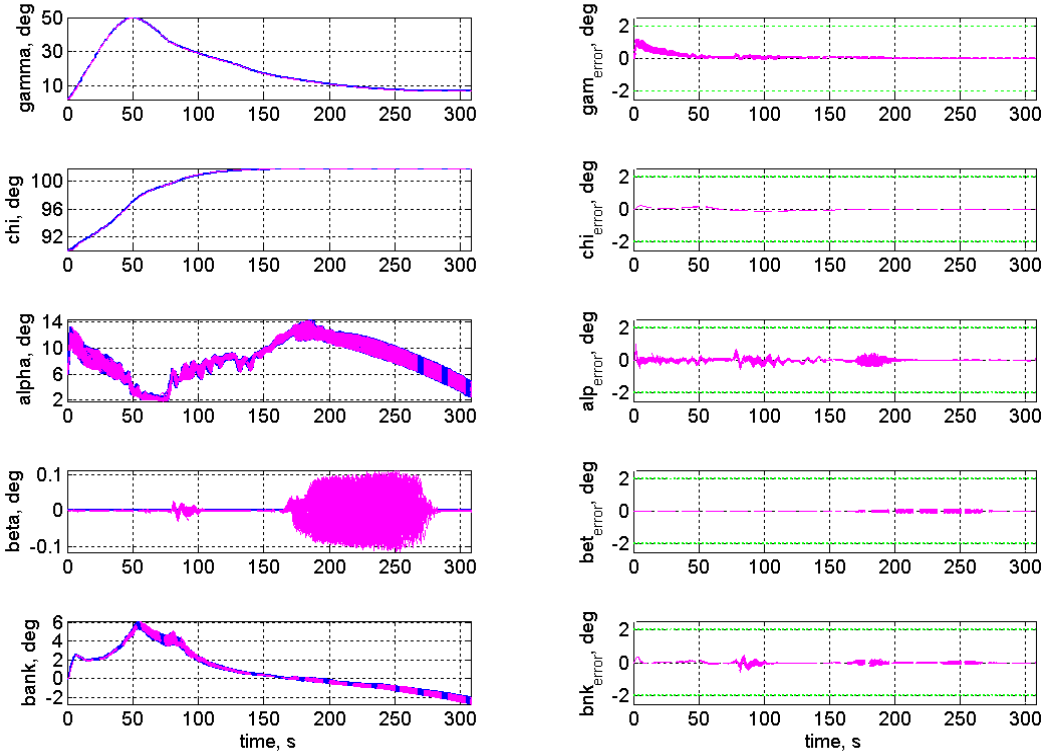

Figure 7 Monte Carlo (300 of 1500 sims): guidance & control tracking signals.

Figure 8 shows the time response of two sets of aerodynamic surface deflections (all with dotted-green lines indicating the magnitude saturation limits). The deflections in the right column, together the rudder deflection at the bottom-left corner of the figure, are the Hopper's physical surface deflections while those in the right column are "fictitious" actuator deflections used for implementation of the Hopper aerodynamic database (corresponding to, for example, $\delta_{eo}=(\delta_{ELO}+\delta_{ERO})/2$ and $\delta_{ai}=(\delta_{ELI}-\delta_{ERI})/2$). It is noted that the optimal trim strategy of the Hopper RLV allows, and even expects, saturation of δ_{ERI}, δ_{ELI} and δ_{FLAP}.

It is seen, based on the last remark above, that the desired control activity objectives are satisfied with only minor (and temporary) saturation of the outboard surfaces δ_{ERO}, δ_{ELO}. Note as well, the progressive aerodynamic surfaces activity reduction in the final stage of the ascent, around the 250 to 300 seconds region. This control surface activity reduction is the result of the requirement to provide loading and heat damage protection for the surfaces as the vehicle speed increases (recall that it was mentioned that the Aerodynamic-Moment-Inversion component included magnitude/rate limit adaptation based on Mach / dynamic pressure). Note also that the rudder deflection is

close to zero through out the ascent flight, this is due to the TVC minimizing the lateral acceleration, and thus keeping sideslip close to zero as desired, using the deflection of the portside engines, see Figure 9.

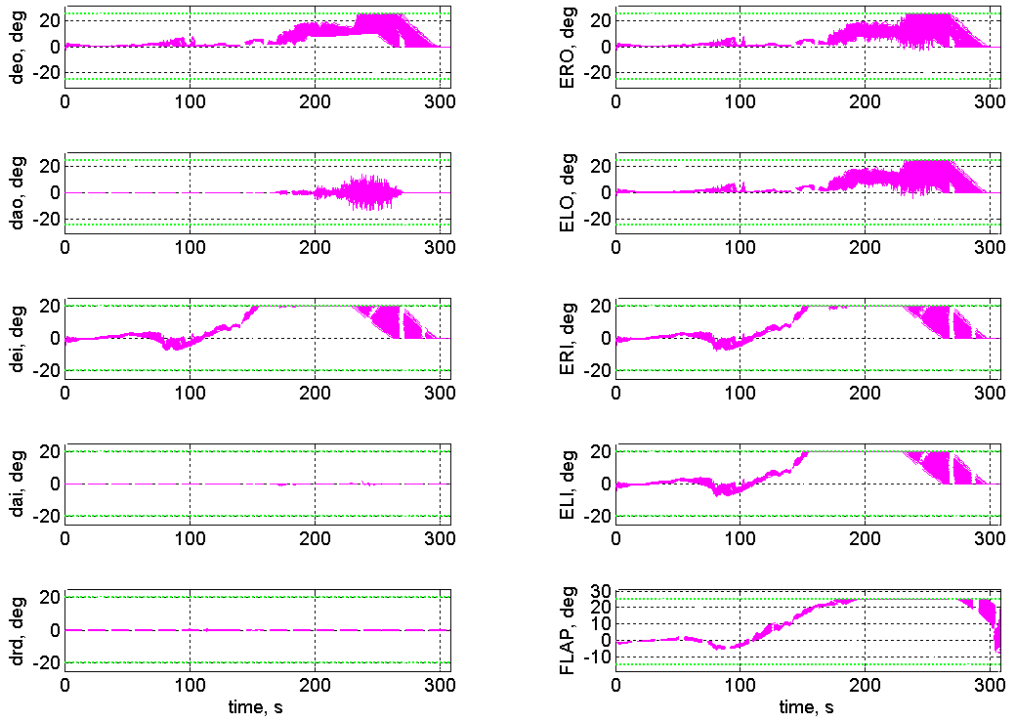

Figure 8 Monte Carlo (300 of 1500 sim): aerodynamic and Hopper surfaces deflections.

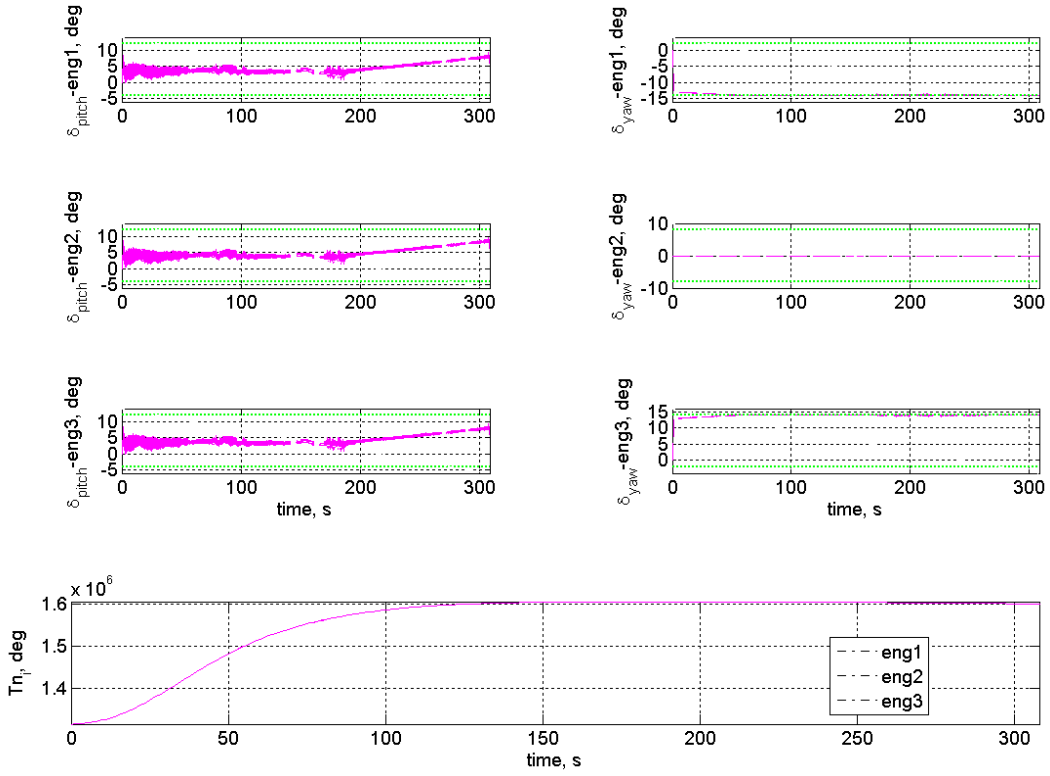

Figure 9 Monte Carlo (300 of 1500 sims): thrust vector control deflections and engine thrust.

Figure 9 shows the TVC gimbal deflections and the thrust provided by each engine. Since the latter engine thrusts are obtained by dividing the total thrust profile given in the reference trajectory in equal parts, the resulting responses are coincident, see the bottom plot of the figure. With respect to the pitch (left) and yaw (right) engine gimbal deflections, first note that it has been mentioned that the G&C design is developed so that the aerodynamic surface activity is smoothly reduced at high speeds (from approximately a flight time of 225 seconds onwards) to avoid damages. Additionally, at this high altitude region the associated reduction in dynamic pressure results in a loss of aerodynamic surface effectiveness. These two considerations imply that final RLV steering must be performed using the engine deflections (and RCS demands). This is especially the case for longitudinal control and is easily appreciated in the left column of Figure 9 that shows the pitch engine deflections increasing in the mid-to-end flight range. Since all engines have the same x-axis coordinate and the same thrust, the engines pitch deflections are almost the same for all of them as observed in the left plots.

For the yaw gimbal deflections shown at the right-plots of Figure 9, and recalling the implementation used in the TVC, it is noted that the two portside engines immediately tend to their maximum magnitude limits but with opposite signs (in trying to zero out the lateral moment). The central engine (engine 2) deflection is not used in this case since the moments and forces produced by the other two are sufficient to compensate the desired allocated moment. Recall that no optimal engine moment allocation is performed, which is reflected in the yaw gimbal actuator activity for the portside engines (clearly not minimized). This can be changed by including standard optimal allocation schemes [4, 5].

Figure 10 shows some additional performance measurements: altitude, Mach, Lift-to-Drag ratio and dynamic pressure time responses for the reference optimized-trajectory (solid blue lines) and for the same 300 MC runs (magenta dashed lines). It is seen that the optimized ascent reference parameters are adequately followed (altitude and Mach are not directly controlled in the present design and thus deviate slightly after a while –but always within a small margin).

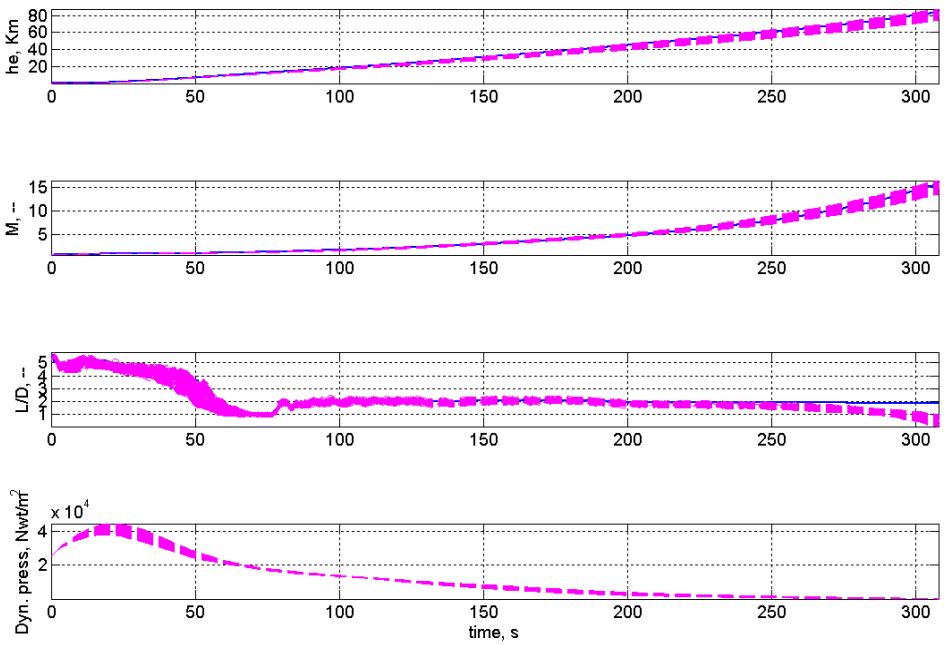

Figure 10 Monte Carlo (300 of 1500 sims): relevant aerodynamic flight parameters

Finally, Table 2 presents a statistical analysis of the MC campaign: maximum error, mean error and mean of the standard deviations for the main G&C parameters. The errors for the heading angle χ, flight path angle γ and lift-to-drag L/D measurements are formed using the reference trajectory values (χ_{ref}, γ_{ref} and L/D_{ref}). The aerodynamic angles errors use as baseline, the guidance-calculated aerodynamic angles (α_{calc}, β_{calc} and σ_{calc}) while the accelerations, airspeed and altitude used the corresponding measurements from the nominal MC run.

Table 2 Main statistical analysis for Monte Carlo campaign.

	Maximum error	Mean errors	Mean of standard deviation error
χ error, deg	0.2304	0.0465	0.0521
γ error, deg	1.1642	0.0912	0.1627
α error, deg	0.9492	0.0582	0.0892
β error, deg	0.1144	0.0107	0.0203
σ error, deg	0.5688	0.0376	0.0575
Lift/drag error, non-dim	2.0986	0.2654	0.2832
x-load factor error, g	0.2091	0.0440	0.0250
y-load factor error, g	0.0055	0.0002	0.0003
z-load factor error, g	0.2463	0.0130	0.0106
V error, m/s	294.8340	48.8821	41.8061
He error, Km	6.3181	1.1044	0.8853

Observe that the guidance and control angle errors satisfy quite well the design objective (of being less than 2 degrees) with even very small mean errors. Similarly, the lift-to-drag ratio (whose error should be close to zero) has small mean error –although its maximum error seems high, note that it occurs at the beginning of the ascent trajectory, the flight period from 0 to 50 seconds, which is when maximum aerodynamic loading occurs Figure 10).

Conclusion

In this article the design of an NDI G&C system for the automated ascent of the Hopper RLV vehicle is presented. The resulting design performance and robustness property are validated, with excellent results, using a Monte Carlo campaign (with realistic aerodynamic mismatch, corrupted measurements, parametric uncertainty and high fidelity atmospheric and DKE dynamics models). NDI technology is used due to programmatic and goal-oriented reasons (i.e. the G&C design is to form part of a closed-loop environment for RLV fault detection and isolation research that requires a certain measure of closed-loop fault tolerance properties –which NDI designs inherently provide).

References

[1] Balas, G.J., Doyle, J.C., Glover, K., Packard, A., Smith, R., "μ-Analysis and Synthesis Toolbox," The Mathworks & MUSYN Inc. June 2001.

[2] Cobleigh, R.B., "Development of the X-33 Aerodynamic Uncertainty Model," NASA TP-1998-206544.

[3] Costa, R.R., Chu, Q.P., Mulder, J.A., "Re-Entry Flight Controller Design using Nonlinear Dynamic Inversion", Journal of Spacecraft and Rockets, Vol. 40, Number 1, 2003.

[4] Durham, W.C., "Computationally Efficient Control Allocation," AIAA Guidance, Navigation and Control Conference, Paper AIAA 99-4214, Portland, August 1999.

[5] Enns, D., "Control Allocation Approaches," AIAA Guidance, Navigation and Control Conference, Paper AIAA 98-4109, Boston, August 1998.

[6] Honeywell and Lockheed Martin. "Application of Multivariable Control Theory to Aircraft Control Laws," Technical Report WL-TR-96-3099, Flight Dynamics Directorate, Wright Laboratory, Wright-Patterson Air Force Base, OH, May 1996.

[7] Ito, J. Georgie, J. Valasek and D.T. Ward, "Re-entry Vehicle Flight Controls Design Guidelines: Dynamic Inversion", Final Technical Report NAG9-1085, 2001.

[8] Kerr, M., Marcos, A., Peñín, L.F., Bornschlegl, E., "Gain Scheduled FDI for a Re-entry Vehicle," AIAA Guidance, Navigation and Control Conference, Hawaii, August 2008.

[9] Niemann, H., Stoustrup, J., "Robust Fault Detection in Open Loop vs. Closed Loop," 36th IEEE Conference on Decision and Control, San Diego, December, 1997.

[10] Marcos, A., Peñín, L.F., Caramagno, A., Sommer, J., Belau, W., “Atmospheric Re-Entry NDI Control Design for the Hopper RLV Concept,” 17th IFAC Symposium on Automatic Control in Aerospace, Toulouse, July 2007.

[11] Mooij, E., Aerospace-Plane Flight Dynamics. Analysis of Guidance and Control Concepts. American Institute of Aeronautics and Astronautics, Washington, 1998.

[12] Ostroff, A.J., Bacon, B.J., “Force and Moment Approach for Achievable Dynamics using Nonlinear Dynamic Inversion,” AIAA Guidance, Navigation and Control Conference, Virginia, August 1999.

[13] Snell, S.A., Nonlinear Dynamic-Inversion Flight Control of Supermaneuverable Aircraft. PhD. Thesis, Dept. Aerospace and Engineering Mechanics, University of Minnesota, October 1991.

[14] Spies, J. “RLV Hopper: Consolidated System Concept” 53rd International Astronautical Congress, Texas, October 2002.

[15] Vu, B.D., “Nonlinear Dynamic Inversion Control,” Chapter 9 in Robust Flight Control: A Design Challenge, Editors Magni, J.F., Bennani, S., Terlouw, J., Lecture Notes in Control and Information Sciences, Springer-Verlag, 1997.